A 40-Year 1-km Daily Seamless Near-Surface Air Temperature Product Over Yellow River Basin of China

Meiling Gao, Huihui Xu, Zhenyu Tan, Zhenhong Li, *Senior Member, IEEE*, and Guijun Yang

***Abstract*—Near-surface air temperature (NSAT) is an important environmental parameter; however, there is a lack of long-term, fine-scale NSAT products that offer complete spatiotemporal continuity. Although several available products cover different periods and regions, obtaining gridded NSAT data outside of the provided regions and periods remains challenging. Using multiple source data (ERA5-Land, global land data assimilation system, remotely-sensed data, and several auxiliary factors), a new high-efficient framework for estimating NSAT is presented using the random forest algorithm and implemented on the Google Earth Engine platform in this study. Thereby, the 1-km daily seamless NSAT product (containing daily maximum, mean, and minimum) from January 1st 1981 to December 31st 2020 over the Yellow River Basin in China is generated. To our knowledge, this is the first product that satisfies the conditions of high resolution, seamless coverage, and long-term continuity simultaneously for the Yellow River Basin. Tenfold cross validation shows that the RMSE, MAE, and R^2 for the maximum NSAT are 1.746–1.932 K, 1.351–1.486 K, and 0.968–0.974, respectively; for the mean NSAT are 1.219–1.354 K, 0.940–1.035 K, and 0.984–0.987; and for the minimum daily NSAT are 1.663–1.732 K, 1.280–1.322 K, and 0.975–0.997. In addition, a user-friendly NSAT estimation tool was developed for the first time, enabling users to derive NSAT products for specific areas and time periods of interest. Evaluation of the tool indicates that the accuracy of temporally extended NSAT is satisfactory, while the accuracy of spatially extended NSAT is lower compared to the original region. The generated long-term finer-scale NSAT product and the developed NSAT estimation tool hold potential benefits for ecoclimate researchers and environmental policy makers.**

***Index Terms*—ERA5-land, global land data assimilation system (GLDAS), remotely-sensed data, Google Earth Engine (GEE), random forest (RF), near surface air temperature (NSAT).**

Manuscript received 19 April 2023; revised 27 June 2023; accepted 25 July 2023. Date of publication 2 August 2023; date of current version 15 August 2023. This work was supported in part by the National Natural Science Foundation of China under Grant 42001382, in part by the Natural Science Basic Research Program of Shaanxi under Grant 2021JQ-238, in part by the Shaanxi Province Science and Technology Innovation Team under Grant 2021TD-51, in part by the Shaanxi Province Geoscience Big Data and Geohazard Prevention Innovation Team (2022), and in part by the Fundamental Research Funds for the Central Universities, CHD, under Grant 300102260301 and Grant 300102262902. *(Corresponding author: Zhenhong Li.)*

Meiling Gao, Zhenhong Li, and Guijun Yang are with the College of Geological Engineering and Geomatics, Chang'an University, Xi'an 710064, China, also with the Big Data Center for Geosciences and Satellites, Chang'an University, Xi'an 710064, China, also with the Key Laboratory of Loess, Xi'an 710054, China, and also with the Key Laboratory of Western China's Mineral Resource and Geological Engineering, Ministry of Education; and Key Laboratory of Ecological Geology and Disaster Prevention, Ministry of Natural Resources, Xi'an 710054, China (e-mail: gaomeiling@chd.edu.cn; zhenhong.li@chd.edu.cn; guijun.yang@163.com).

Huihui Xu is with the College of Geological Engineering and Geomatics, Chang'an University, Xi'an 710064, China, and also with the Big Data Center for Geosciences and Satellites, Chang'an University, Xi'an 710064, China (e-mail: huihui.xu@chd.edu.cn).

Zhenyu Tan is with the College of Urban and Environmental Sciences, Northwest University, Xi'an 710127, China (e-mail: tanzhenyu@nwu.edu.cn).

Digital Object Identifier 10.1109/JSTARS.2023.3301146

I. Introduction

NEAR-SURFACE air temperature (NSAT) typically refers to the air temperature measured 1.5–2.0 m above a surface. A high-accuracy and fine-scale seamless NSAT product can be valuable for various environmental applications. For example, NSAT is widely utilized in assessing responses to global warming [1], [2] and the impacts of drought hazards [3]. It can provide supplementary information for intelligent agriculture [4] and plays a crucial role in evaluating urban ecological environments [5], [6]. The significance of NSAT as an essential parameter in earth system-related studies has increased in recent years. In addition to mean NSAT, which is commonly used at different spatial or temporal scales, extreme NSAT is also of great importance. For instance, the daily NSAT range, calculated as the difference between the daily extreme maximum and the daily extreme minimum NSAT, significantly affects plant growth [7].

Several methods can be used to obtain the extreme and mean NSAT. In situ measurements are a traditional method for acquiring NSAT with higher accuracy [8]. However, the sparse distribution of in situ observation stations limits its application over large-scale regions. Thus, several methods have been developed to derive the spatial distribution of NSAT [9], [10], [11], [12], [13], [14]. Mapping the spatial distribution of NSAT based on remotely-sensed land surface temperature (LST) and auxiliary variables becomes a valid method because NSAT and LST correlate strongly, and satellite sensors can easily provide gridded LST [9], [15], [16]. For example, Dos Santos [17] estimated the daily maximum air temperature in London using machine learning and MODIS LST data. Shen et al. [18] mapped the daily air temperature over China using a deep belief network based on MODIS LST. Zhang et al. [9] estimated hourly NSAT by blending geostationary datasets from the two-satellite system of the GOES-R series. However, most of these previous studies covered only short-time periods, typically one year, and their products were spatially discontinuous due to missing remotely-sensed LST pixels [9], [18], [19]. The NSAT products retrieved through remotely-sensed LST usually have

finer spatial scales, but cloud contamination of the original LST data often results in the NSAT not being spatially continuous unless a remedial strategy is adopted to extrapolate the missing pixels.

Besides the methods based on satellite-derived LST with auxiliary variables for NSAT estimation, simulation with dynamic models [20], [21] is also an efficient way to retrieve NSAT. For example, global land data assimilation system (GLDAS) encompasses an enormous archive of modeled and observed global and surface meteorological data, parameter maps, and output. It includes 1° and 0.25° resolution simulations of several different land surface models, from which NSAT can be obtained [22]. ERA5-land (land component of the fifth generation of European Re-Analysis) is a global dataset published by European Centre for Medium-Range Weather Forecasts (ECMWF) that contains NSATs with a spatial resolution of 0.1° and a temporal resolution of 1 h [23]. The China Meteorological Forcing Dataset contains several meteorological parameters, including NSAT, with a resolution of 0.1° and a temporal resolution of 3 h [24]. Many other datasets also provide the 2-m temperature product, such as CLDAS [25] and NCAR-NCEP reanalysis datasets [26]. Such NSAT products usually cover a long period and update regularly, and they are seamless in space and have a fine-grained temporal interval. However, their spatial resolutions are relatively coarse (e.g., 0.1° for ECMWF and 0.25° for GLDAS products). These coarse resolutions for NSAT are insufficient for recognizing details in regional related applications.

The methods for retrieving NSAT based on satellite-derived LST often suffer from spatial discontinuity caused by cloud contamination or sensor issues, while reanalysis or modeling products tend to have coarse spatial resolutions. Consequently, some researchers have explored using gap-filled LST to estimate NSAT [19] or downscaled reanalysis and modeling datasets [10]. Recent studies have started to estimate NSAT by combining remotely-sensed LST with modeling or reanalysis products instead of relying on a single LST source [27], [28], [29]. Numerous studies have focused on developing NSAT estimation models and generating products with finer spatial resolutions and shorter temporal intervals, covering longer periods. For instance, Chen et al. [27] developed a 1-km daily averaged surface air temperature product over mainland China for 2003–2019 using MODIS LST and GLDAS datasets. Fang et al. [30] combined in situ data, remotely-sensed data, and reanalysis data to retrieve the 0.1° daily maximum, minimum, and mean NSAT in China from 1979 to 2018. Zhang et al. [29] generated the 1-km daily mean air temperature for the Tibetan Plateau from 1980 to 2014. However, to our knowledge, it remains challenging to find an NSAT product that simultaneously satisfies the requirements of high spatial resolution (e.g., 1-km), small temporal intervals (e.g., daily), spatial-temporal seamlessness, coverage of long-term periods, and inclusion of both extreme and mean values. Furthermore, the existing products are not easily extendable to other time periods and regions, leaving users with limited options until the release of new versions. Therefore, there is a need to provide an accessible tool for users.

Considering that the Yellow River Basin of China has been identified as a national priority for ecological protection, the variations in extreme and mean air temperature hold significant importance for the ecological functions of the basin. This study focuses on addressing the aforementioned gaps within this particular basin. The main objectives of this study are as follows: 1) establishing a new technical framework for estimating NSAT and generating a 1-km daily extreme and mean NSAT product for the period of 1980–2020 over the Yellow River Basin Region of China; and 2) developing a user-friendly tool for generating NSAT for different time periods and regions.

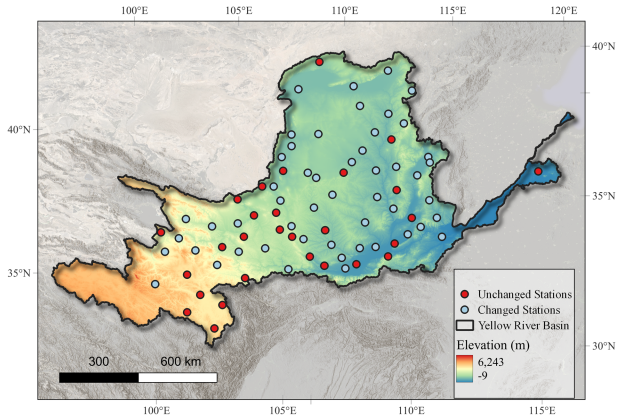

Fig. 1. Map of the Yellow River Basin (in situ observations from 2020 depicted as small points. Stations that have maintained their locations since 1981 are represented by red points, while stations that have changed locations at least once since 1981 are denoted by blue points).

The rest of this article is structured as follows. Section II describes the data and methods used to produce the NSAT. Section III provides a brief overview of the results and analysis of the NSAT product. Section IV presents the generated dataset and the NSAT estimation tool. Section V include the discussion. Finally, Section VI concludes this article.

II. Materials

A. Study Region

The Yellow River Basin (E 96°–119°, N 32°–42°) is a region impacted by Yellow River geographically and ecologically. It spans across nine provinces of China, as depicted in Fig. 1. The western part of the region exhibits higher elevations compared to the eastern part, creating a significant height disparity between the two. The Yellow River Basin is characterized by numerous mountains and distinctive landforms that vary across different areas within the basin. Moreover, due to its location in the middle latitude region, the basin experiences complex atmospheric and monsoon circulation patterns, resulting in diverse climates across its different sections. In addition, it is worth noting that the Yellow River Basin is recognized as one of the most vulnerable areas in China [31].

B. Methodology

In generating the 40-year extreme and mean NSAT with finer spatial and temporal resolution, it is important to consider computational cost and data storage. The Google Earth Engine

TABLE I
DATA SOURCES USED FOR 1-KM DAILY NSAT PRODUCT GENERATION

Variables	Data sources
NSAT	In situ observation
LST	GLDAS/ERA5-Land
Downward shortwave radiation	GLDAS/ERA5-Land
Downward longwave radiation	GLDAS/ERA5-Land
Specific humidity	GLDAS/ERA5-Land
Precipitation speed	GLDAS/ERA5-Land
Wind speed	GLDAS/ERA5-Land
NDVI/EVI	NOAA_AVHRR NDVI before February 2000, and MODIS EVI since February 2000
Population	GHSL dataset for period before 2000, and GPWv4 since 2000
DEM	MERIT DEM for period before 2000, and NASA SRTM since 2000
Slope	Calculated by DEM
Others	Longitude, Latitude, Year, Month, Day of Year (DOY)

(GEE) is a platform for cloud computing containing abundant geospatial datasets [32]. Utilizing GEE can help overcome limitations associated with limited local computing resources. Therefore, in this study, the GEE platform was utilized to produce the NSAT product.

Five different types of data were collected for the NSAT estimation model, including in situ observations, population datasets, remotely-sensed products, model simulations or reanalysis products, as well as location and time information. The study period spanned from January 1st, 1981 to December 31st, 2020. Since a single data source might not cover the entire period, multiple data sources for specific variables were utilized in this study. All data types, except for in situ observations and location and time information (longitude, latitude, year, month, and day of the year), were obtained directly from GEE. Further details regarding the variables are provided in Table I.

The in situ stations (see Fig. 1) offered the NSAT observations for model training and accuracy evaluation. The data were obtained from the China Meteorological Data Service Center (http://data.cma.cn/en), which offers daily maximum, mean, and minimum NSAT data. It is important to note that the precise locations of some stations used in the study changed during the study period, as indicated by the blue points in Fig. 1.

Both the GLDAS [22] and ERA5-Land [23] products offer various near-surface and surface parameters. In this study, we utilized LST, longwave radiation, shortwave radiation, humidity, wind speed, and precipitation speed from these products to estimate NSAT. Previous research has shown that these parameters exhibit a higher correlation with NSAT [15], [18]. The GLDAS parameters have a spatial resolution of 0.25° and a temporal resolution of 3 h, while the ERA5-Land data have a spatial resolution of 0.1° and a temporal precision of 1 h. Due to different versions of the GLDAS product covering different periods, GLDASV2.0 was utilized prior to 2000 and GLDASV2.1 was employed after 2000. The entire study period 1981–2020 can be covered by the ERA5-Land product.

In addition, the vegetation index and DEM from remotely-sensed sources were taken to provide additional information. The MOD13A2 product, which contains enhanced vegetation index (EVI) data with a spatial resolution of 500-m and a temporal resolution of 16 days, selects the best pixel values within the 16-day period to enable high data quality. MODIS EVI was utilized in this study; however, it was unavailable before February 2000. Therefore, the gap was filled using the normalized difference vegetation index (NDVI) from several NOAA AVHRR sensors [33]. The NOAA NDVI dataset was generated daily on a 0.05° global grid. For DEM data, the multi-error-removed-terrain (MERIT) dataset [34] was used for the period 1981–1999, while NASA SRTM [35] was used for the period after 2000. The slope calculations in this study relied on the DEM data.

Population was also used in this study. The global human settlement layer (GHSL) population grid datasets[1] provided information on population distribution and density at a spatial resolution of 250-m for reference epochs in 1975, 1990, 2000, and 2015. For the years 1981–1999, population information was obtained from the GHSL databases, while population data after 2000 was sourced from the gridded population of the world version 4.11 (GPWV411) dataset.[2] The GPWV411 dataset models the global human population distribution for the years 2000, 2005, 2010, 2015, and 2020, using 30 arc-second (approximately 1-km) grid cells.

The machine learning algorithm is frequently utilized for NSAT estimation and has demonstrated satisfactory performance in NSAT assessment [15], [27]. In a previous study, we compared the deep neural network with the random forest (RF) algorithm, and the results suggested that RF can achieve optimized accuracy with less computation [15]. Thus, the RF approach was selected for this study. RF is an ensemble machine learning algorithm based on decision trees that can be used for classification or regression problems [36]. The final prediction result is obtained by voting for classifications or taking the mean value of the independent decision trees for regression. After validation, we used 100 decision trees for the following.

The tenfold cross-validation method [37], [38] was used to obtain robust estimations of the model results. Specifically, the dataset was divided into ten equal-sized subsets. The model was trained ten times, with nine subsets used as the training set and the remaining subset as the validation set in each iteration. After each iteration, the predicted results from each iteration were collected, and these results were used to calculate the overall performance after the ten iterations.

[1][Online]. Available: https://developers.google.com/earth-engine/datasets/catalog/JRC_GHSL_P2016_POP_GPW_GLOBE_V1

[2][Online]. Available: https://developers.google.com/earthengine/datasets/catalog/CIESIN_GPWv411_GPW_Land_Area

C. NSAT Estimation Scheme Design

The flowchart for the NSAT estimation designed in this study contains the following steps.

1) Data collection and processing: Initially, the station-related information, including the in situ observed NSAT and its corresponding location and time, was uploaded to GEE. Simultaneously, all the variables listed in Table I were preprocessed to ensure a consistent spatial and temporal resolution, specifically 1-km for spatial resolution and daily for temporal resolution. To be more specific, nearest-neighbor resampling was used to achieve a 1-km spatial resolution if the original resolution was not 1 km. The linear interpolation method was employed for variables with a temporal resolution lower than daily. Variables with an original temporal resolution higher than daily were merged to obtain daily values. In addition, there were a few missing data entries for the EVI product, which were filled using the S–G filter method [39]. For variables that changed only minimally over time, such as DEM, slope, and population, the data closest to the prediction time were used. The input data point values were extracted from GEE based on the observed locations and times, and then the extracted data points, along with the observed NSAT at the corresponding location and time, constituted the model input and output during the training period. Due to some variables not covering the entire 40-year period, the study period was divided into two stages: the period from January 1st, 1981 to December 31st, 1999 (referred to as "the period before 2000" for brevity) and the period from January 1st, 2000 to December 31st, 2020 (referred to as "the period after 2000" for brevity).
2) NSAT estimation model establishment: The RF regression model utilized multiple input variables listed in Table I, excluding NSAT which served as the ground truth for model output. Four models were established with different input schemes. Model 1 in Fig. 2 used GLDAS sources to estimate NSAT, while Model 2 used ERA5-Land data as input. Model 3 combined the GLDAS and ERA5-Land data as input for the RF model, and Model 4 combined the results of the first and second models by calculating the mean estimates for mean, maximum, and minimum NSAT. Among these four models, all variables except LST, downward shortwave radiation, specific humidity, precipitation speed, and wind speed were the same. The tenfold cross-validation method was employed to evaluate the four NSAT estimation models.
3) Subsampling strategies: Increasing the number of data samples can provide additional information on the relationship between model inputs and outputs. However, the RF model training on GEE is limited to a data size of 100 MB. All the samples from the 40-year period over the Yellow River basin, used as a training dataset, are too large for GEE free users. Thus, it is necessary to subsample the input data to reduce the sample size beforehand. Therefore, we considered dividing all the samples into several groups, with each subgroup regarded as an independent training dataset for generating the corresponding NSAT. Three subsampling strategies were designed and compared in this study. Previous studies have found that station density is positively related to the accuracy of prediction of air temperature [40]. Hence, all the stations were involved with model training. The first subsampling strategy is the Year-based Subsampling Strategy (YSS), which involves using only the closest two-year samples during each two-year period. For example, the samples from 1981 and 1982 form a training group, and the model trained on this dataset is used to generate NSAT for those two years. The second strategy is the month-based subsampling strategy (MSS), where each month over the 20 years is selected as a group. For instance, all samples from January of 1981, 1982, …, 1999 are used as a training group, and the model trained on this group generates NSAT for January from 1981 to 1999. The final strategy is the year–month combined subsampling strategy (YMSS), which utilizes samples from the prediction months of the ten closest years, as well as samples from all months of the prediction year. For example, the samples from the entire year of 1981 and the samples from January of 1981–1990 are used for training and generating NSAT for January 1981. All three strategies consist of a similar number of samples, approximately 50 000 records for each training.
4) NSAT generation and analysis: After optimizing the model for online NSAT estimation, a 40-year NSAT product was generated for the Yellow River Basin Region, including maximum, minimum, and mean NSAT. The spatial-temporal variation of NSAT was analyzed using Mann–Kendall (M–K) trend detection [41] and the Sen's Slope [42] method. The nonparametric M–K test is suitable for testing the presence of increasing or decreasing trends, while Sen's Slope can quantify the magnitude of the trend. The combination of M–K trend detection and Sen's Slope is commonly used in temporal trend analysis and was employed in this study to detect NSAT variations from 1981 to 2020.

D. Development of NSAT Estimation Tool

Although long-term NSAT products have been released by several researchers, accessing data beyond the coverage of these products is challenging for users. To address this issue, a flexible and convenient NSAT estimation tool based on GEE was developed. The tool utilizes a pretrained model for periods without any observation. After the development of the estimation tool, its accuracy was evaluated from both temporal and spatial perspectives. The overall flowchart of this study is depicted in Fig. 2.

III. Results and Analysis

A. Evaluation of NSAT Estimation Models

All the predicted NSAT and observed NSAT are distributed around the 1:1 line in different models, as shown in Fig. 3.

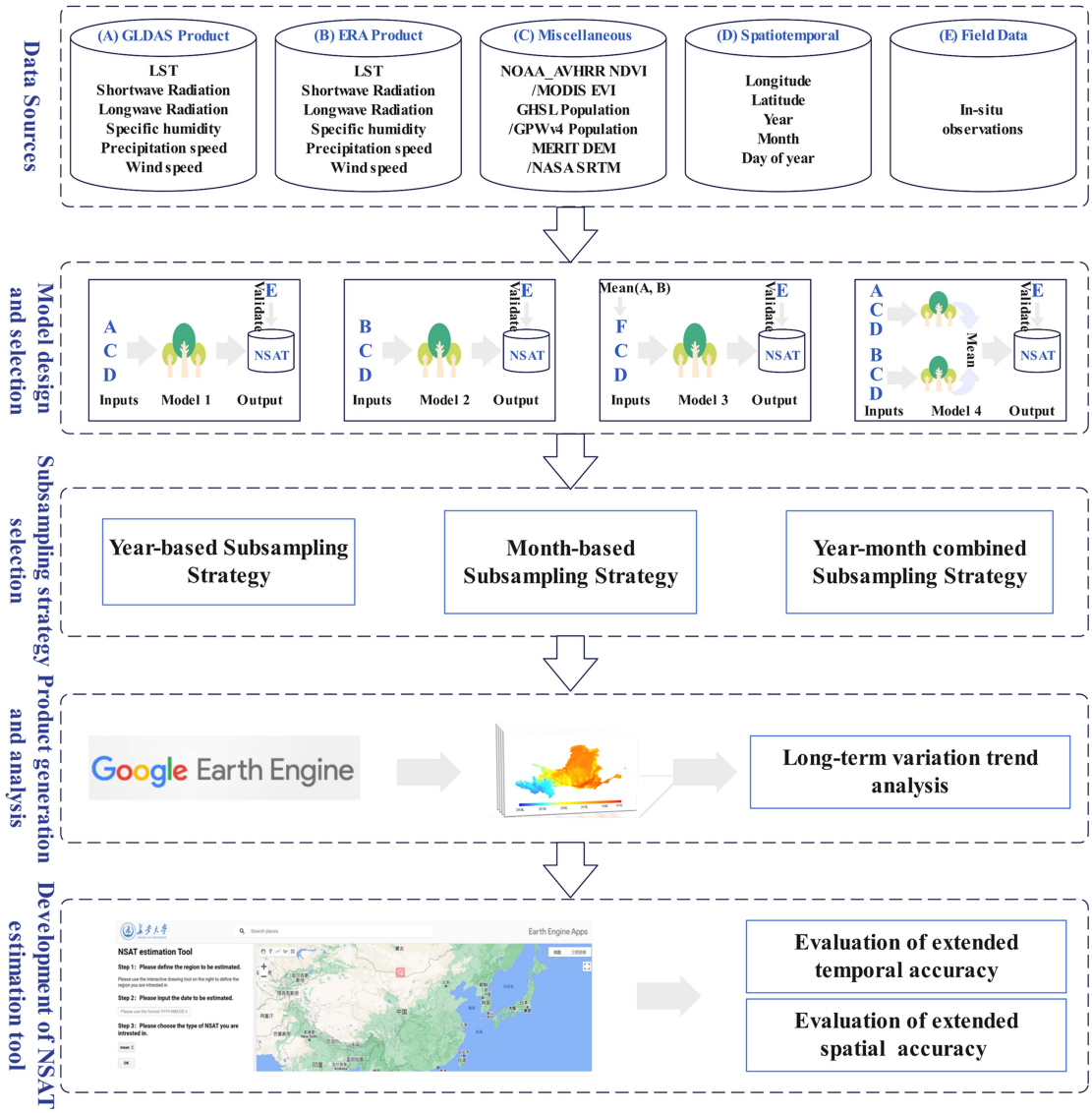

Fig. 2. Flowchart of this study.

The first three rows present the accuracy comparison for the period before 2000. Fig. 3(b), (f), and (j) indicates that Model 2, which uses ERA5-Land data, has higher accuracy when estimating maximum, mean, and minimum NSAT compared to the other three estimation models for the time period prior to 2000. Different models show similar R^2 values for mean NSAT estimation, ranging from 0.97 to 0.98, while the lowest MAE and RMSE among the four models are observed in Model 2 at 1.05 K and 1.38 K, respectively. The performance of Model 1 for maximum NSAT estimation is less reliable than that of the other three models. These three models, except for Model 2, show similar accuracy, while Model 2 remains the most reliable with an R^2 of 0.97, MAE of 1.54 K, and RMSE of 2.00 K. The accuracy of minimum NSAT estimation based on Model 1 is also lower than that of Model 2-4, while the R^2 of Models 2–4 is the same. The lowest MAE (1.33 K) and RMSE (1.75 K) for minimum NSAT are observed in Model 2. Therefore, utilizing ERA5-Land data as input is the most advantageous choice for estimating NSAT before 2000. Mean NSAT demonstrates higher accuracy compared to extreme NSAT, and the accuracy of minimum NSAT is higher than that of estimated maximum NSAT.

Fig. 3(m)–(x) presents the accuracy comparison results for the period 2000–2020. Based on a tenfold cross-validation evaluation, Model 4 (combining outputs for Models 1 and 2) demonstrates the best performance in estimating maximum, mean, and minimum NSAT. Therefore, Model 4 can be considered the superior model for NSAT estimation after 2000. The R^2 value of Model 4 for each type of NSAT estimation exceeds 0.97. The MAE for maximum, mean, and minimum NSAT is 1.43 K, 0.923 K, and 1.27 K, respectively, based on Model 4, while the RMSE is 1.84 K, 1.19 K, and 1.65 K, respectively.

For the periods before and after the year 2000, mean NSAT demonstrates higher accuracy, followed by minimum NSAT,

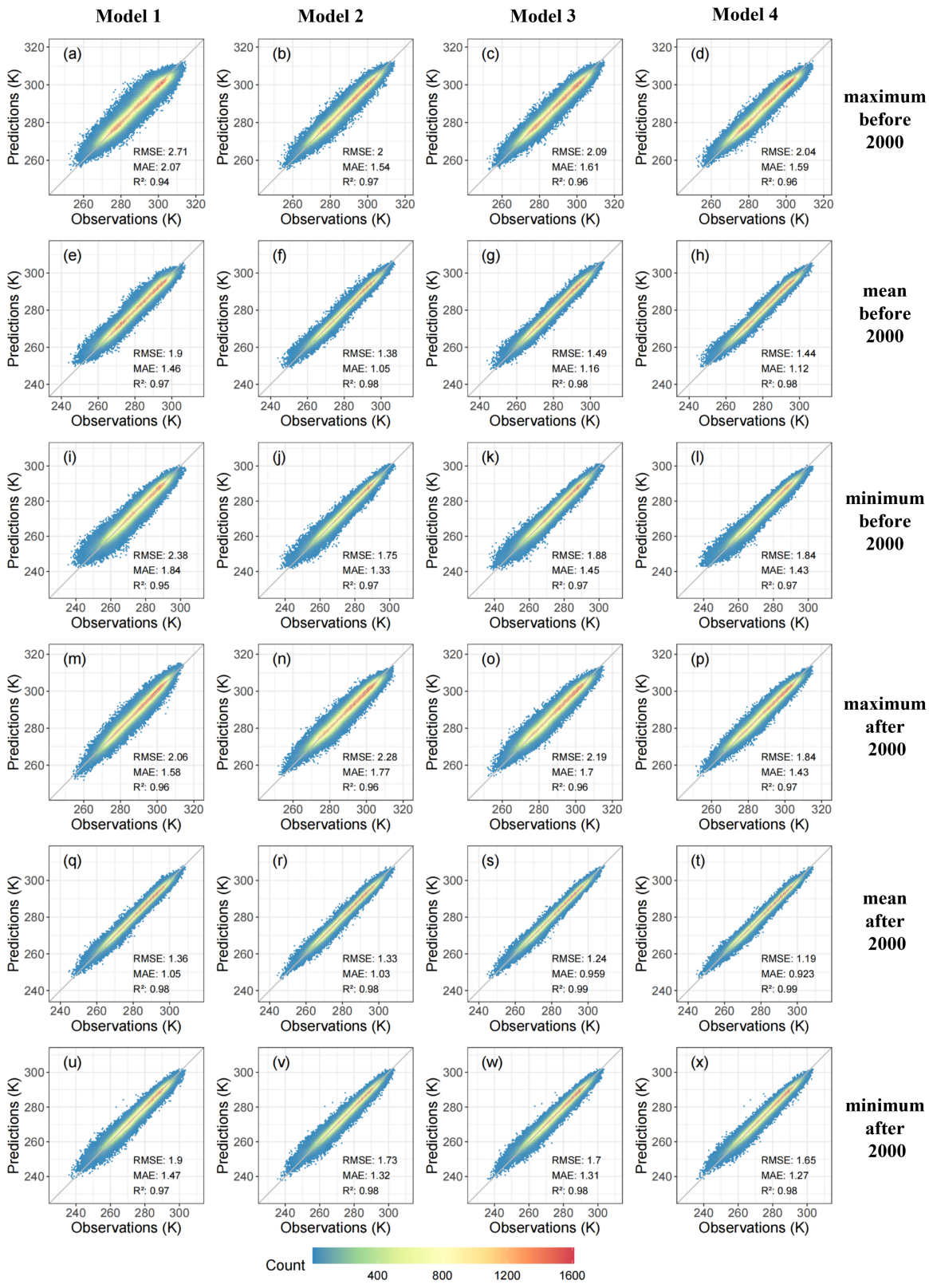

Fig. 3. Accuracy of NSAT estimation using different methods during the periods (a)–(l) 1981–1999 and (m)–(x) 2000–2020. Columns one, two, three, and four correspond to model 1, model 2, model 3, and model 4 in Fig. 2, respectively. Furthermore, rows one and four represent maximum NSAT, rows two and five represent mean NSAT, while rows three and six represent minimum NSAT.

TABLE II
VALIDATION RESULTS OF DIFFERENT SUBSAMPLING STRATEGIES

		RMSE(K)			MAE(K)			R^2		
		YSS	MSS	YMSS	YSS	MSS	YMSS	YSS	MSS	YMSS
Mean	Period1	1.376	**1.354**	1.360	1.053	**1.035**	1.041	0.984	**0.984**	0.984
LST	Period2	1.230	**1.219**	1.223	0.950	**0.940**	0.944	0.984	**0.987**	0.987
Maximum	Period1	**1.932**	1.937	1.938	**1.486**	1.492	1.492	**0.968**	0.968	0.968
LST	Period2	**1.746**	1.783	1.774	**1.351**	1.387	1.378	**0.974**	0.973	0.973
Minimum	Period1	1.788	**1.732**	1.742	1.366	**1.322**	1.330	0.973	**0.975**	0.975
LST	Period2	1.700	**1.663**	1.674	1.308	**1.280**	1.289	0.976	**0.977**	0.977

Period1: the period before 2000, Period2: the period after 2000
The bold values used to highlight the best indicators.

while estimating maximum NSAT is the most challenging. Estimating accurate mean NSAT is easier than estimating accurate extreme NSAT, which aligns with previous studies [30], [43] indicating that mean NSAT has higher precision than extreme NSAT. In addition, ERA5-Land and GLDAS data have also shown cold biases in some regions [20], making it unlikely to achieve the same high accuracy for maximum NSAT as for the others. Furthermore, the bias of NSAT after 2000 is smaller than that before 2000, although the differences are minimal. Comparing the best estimated results for the two periods (i.e., Model 2 before 2000 and Model 4 after 2000), the differences in R^2, MAE, and RMSE for maximum NSAT are 0.00, 0.11 K, and 0.16 K, respectively. The differences in R^2, MAE, and RMSE for mean NSAT are 0.01, 0.1 K, and 0.19 K, while the differences for minimum NSAT between the two periods are 0.01, 0.06 K, and 0.1 K, respectively. The accuracy of the original input product may be the main reason for the differences observed between the two periods. From the first column of Fig. 3(a), (e), (i), (m), (q), and (u), it can be observed that Model 1 shows noticeable differences in accuracy before and after 2000. However, the second column of Fig. 3(b), (f), (j), (n), (r), and (v) demonstrates that the accuracy of Model 2 remains stable across different periods. This can be attributed to the utilization of different versions of the GLDAS product: GLDASV2.0 was used before 2000, while GLDASV2.1 was employed after 2000, as explained in Section II-B. In contrast, the ERA5-Land input utilized throughout the study period remains consistent. Consequently, the model utilizing GLDAS-related input exhibits varying performance before and after 2000, whereas the model using only ERA5-Land input (Model 2) maintains consistent performance.

Based on the aforementioned results, Model 2, which relies on ERA5-Land data, is chosen for each NSAT type for the period before 2000. Meanwhile, Model 4 is utilized for NSAT estimation after the year 2000.

B. Comparison of Subsampling Strategies

To reduce the sample size to fit into the GEE platform, three subsampling schemes were designed, as described in Section II. The validation results of these three strategies using the tenfold cross-validation method are presented in Table II. For mean NSAT estimation, the MSS strategy exhibits lower RMSE and MAE values while achieving a higher R^2 compared to the other two strategies. This finding confirms that MSS is the optimal subsampling strategy for mean NSAT estimation for both periods, before and after the year 2000. The MSS strategy also yields smaller RMSE and MAE values for minimum NSAT estimation compared to YSS and YMSS while maintaining the maximum R^2 for both periods. Besides, the YSS strategy achieves the lowest RMSE and MAE values, along with the highest R^2, for maximum NSAT estimation in both periods. Thus, the MSS is employed for estimating the mean and minimum NSAT, while the year-based approach is utilized for estimating the maximum NSAT.

Some previous research works have also estimated 1-km daily mean NSAT, focusing on the study period mainly distributed after 2000, and in which the RMSEs are larger than 1.7 K over different regions [28], [29], [44]. The MAE is 1.57 K over the Yangtze River Basin by Li et al. [28], while Chen et al. [27] estimated higher accuracy daily mean NSAT over mainland China for 2003–2019 with an RMSE of 1.010 K. The results after 2000 set out in Table II indicate accuracy under the MSS strategy to be higher or similar to that of previous studies, applying the same spatial and temporal resolutions. In addition, Fang et al. [30] showed that the RMSE ranged from 0.35 to 1.0 K for China with the same temporal resolution but its spatial resolution is lower than this study.

RMSE is 1.663 K for minimum NSAT, while MAE is lower than 1.280 K and R^2 is larger than 0.977 after the year 2000. Meanwhile, RMSE is 1.746 K for maximum NSAT, while MAE is 1.351 K and R^2 is larger than 0.974 for the period after 2000. Previous studies [19] regarding the minimum NSAT in mainland China from 2003 to 2016 showed that the RMSE and MAE were 1.82 K and 1.30 K, respectively, while the RMSE and MAE of maximum NSAT were 1.75 and 1.22 K. This accuracy is similar to that achieved in this study, applying identical spatial and temporal resolutions. Moreover, the RMSE regarding the daily maximum NSAT in Dos Santos [17] was 2.03 K, while MAE was 1.6 K and R^2 was 0.68. Shen et al. [18] reported an RMSE of 1.996 and an MAE of 1.539 for 0.01° daily maximum NSAT across China in 2015. Accuracy after 2020 in our study is higher than that for maximum NSAT estimation.

C. Long-Term Variation Analysis of Extreme and Mean NSAT

M–K testing and Sen's Slope were employed to detect the long-term variation trend of NSAT across the Yellow River Basin. The trend is determined by combining the z-score and

TABLE III
DEFINITION OF CHANGE TREND OVER THE PAST 40 YEARS

Slope	|Z|	Variation trend of NSAT
>0.05	>1.64	Significant increase
>0.05	<=1.64	Slight increase
-0.05–0.05	>1.64 | <=1.64	Stable
<-0.05	<=1.64	Slight decrease
<-0.05	>1.64	Significant decrease

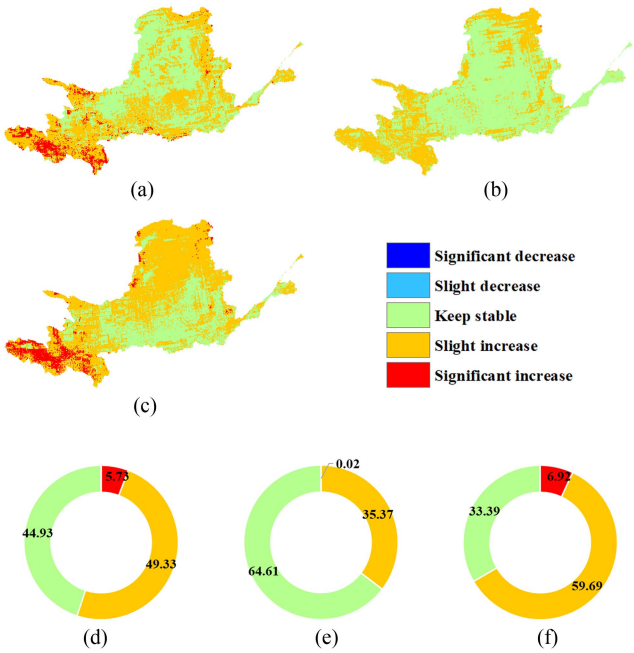

Fig. 4. Long-term variation trend of maximum, mean, and minimum NSAT over the period 1980–2020. (a)–(c) Spatial distributions and (d)–(f) are the statistics (Unit: %) of the trend. (a) Maximum NSAT. (b) Mean NSAT. (c) Minimum NSAT. (d) Maximum NSAT. (e) Mean NSAT. (f) Minimum NSAT.

the slope, and it is classified into five types in this study (i.e., significant increase, slight increase, stable, slight decrease, and significant decrease), as outlined in Table III. The spatial distribution of the variation trend and the corresponding statistics are presented in Fig. 4. The western part of the region exhibits a significant increasing trend for extreme NSAT [see Fig. 4(a) and (c)]. Areas with a slight increase in maximum NSAT are dispersed throughout the basin. The north of the basin primarily experiences a slight increase in minimum NSAT, while the southeastern region shows a predominantly stable pattern for minimum NSAT. For mean NSAT, most areas remain stable [see Fig. 4(b)], with a slight increase observed in the western and northern parts of the basin over the past 40 years. The statistical findings indicate that over half of the region demonstrates an increasing trend in maximum NSAT and minimum NSAT Specifically, the maximum and minimum NSATs slightly increase over 49.33% and 59.69% of the entire region, respectively. Areas with a significant increase account for 5.73% and 6.92% for maximum and minimum NSAT, respectively. In comparison to extreme NSAT, the variation in mean NSAT is less pronounced, with only 35.37% of the region displaying a slight increasing trend. It is important to note that the extreme and mean NSAT used in this study refer to the annual mean temperature calculated from daily NSAT data. All daily data have been included in this trend analysis to mitigate biases resulting from limited samples. However, the accuracy of the NSAT product may influence the results of the trend analysis. It can be concluded that the NSAT variation trend exhibits significant spatial heterogeneity. Areas with stable maximum NSAT are often associated with a low slope (see Fig. 1). This trend may be influenced by various factors, including slope, land cover, climate changes, human activities, etc. [45], [46], [47].

IV. DATA PRODUCT AND NSAT ESTIMATION TOOL

A. Data Assets

The daily 1-km NSAT products, spanning from January 1st, 1981 to December, 31st, 2020, containing mean, maximum, and minimum NSAT over the Yellow River Basin Region of China, are available at GEE assets (https://code.earthengine.google.com/c720b7c61c5da99ab5669b2ab70ca7df) for public sharing. Users can use and preprocess the product on the GEE platform directly. Besides, the product is also available from http://doi.org/10.5281/zenodo.7693853.

B. NSAT Estimation Tool

The product provided here relates to NSAT data for a specific period and specific region. For periods or regions outside the product coverage, it is not easy for users to acquire consistent NSAT data, potentially limiting related applications. Hence, we have developed an easy-to-use tool named the "NSAT estimation Tool," which can be used to flexibly estimate NSAT over an extended time period or region. The model instantiated in the tool is based on training data from the Yellow River Basin region and covers the period prior to December 31st, 2020. Users can use this tool to produce data after 2020 and outside the Yellow River Basin using the trained model. The NSAT estimation tool is effective when simultaneously extending the product spatially and temporally.

The NSAT estimation tool is available and publicly accessible as a GEE App: https://meilinggao888.users.earthengine.app/view/nsatestimation. The user interface (UI) of the app is shown at Fig. 5. Three steps are necessary to produce NSAT data. First, users should utilize the interactive tools provided by GEE to define the region of interest. Second, users should input the predicted date in the format "YYYY-MM-DD" (YYYY: year, MM: month, DD: day). Third, the type of NSAT should be selected. Three options are available (i.e., "max," "mean," and "min"), representing the daily maximum, daily mean, and daily minimum NSAT, respectively. After completing the above three steps, the "OK" button should be clicked and the NSAT will be generated. The predicted NSAT will be displayed in the right-hand window as soon as the estimation is complete, whereupon users can export the estimated NSAT image to their own GEE Assets or Google Drive.

The NSAT estimation tool enables users to estimate daily maximum, mean, and minimum NSAT for customized regions

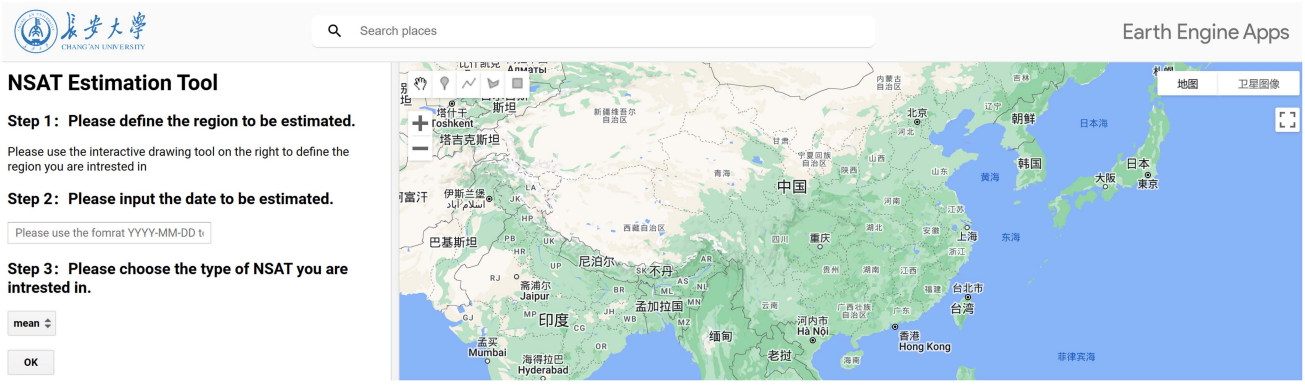

Fig. 5. UI of NSAT estimation tool.

and periods, which can substantially extend the product spatially and temporally. To evaluate the tool's accuracy outside the region and period of our NSAT product, it is analyzed temporally and spatially in Section V.

V. Discussion

A. Model Accuracy With Different Numbers of Input Variables

In the above NSAT estimation, all variables listed in Table I are used as inputs for the estimation model. To test if it is necessary to input all the variables, we ranked the importance of the 15 variables based on the feature importance assessment of the RF algorithm. We then tested the influence of different numbers of input variables on the model's estimation accuracy. Using Model 1 and Model 2 as examples during the period of 2000–2020, the accuracy test results are shown in Fig. 6. The label "3" for "number of input variables" indicates that only the three variables with the highest importance were included, while the label "15" signifies the inclusion of all variables in Fig. 6. It can be observed that with fewer input variables, the RMSE and MAE increase, while the R^2 decreases. Both Model 1 [see Fig. 3(b), (d), and (f)] and Model 2 [see Fig. 3(a), (c), and (e)] indicate that using all 15 variables as input yields the highest accuracy for maximum, minimum, and mean NSAT estimation. Therefore, we included all the variables listed in Table I as input for NSAT product generation. In addition, we tested the variables' sensitivity based on the relevance ranking in a previous study [15], which focused on monthly NSAT estimation based on MODIS LST. The results were consistent with this study's ranking of the variables by importance. Thus, all the selected variables should be included to obtain accurate model estimation results.

B. Accuracy Evaluation for Temporal Extension

In order to evaluate the accuracy of the NSAT predicted by the NSAT estimation tool outside the period covered by our NSAT product, in situ observations from January 1st, 2021 to September 30st, 2021 were collected. The R^2 closely approximated to 1 for the temporally extended NSAT product [see Fig. 7(a)–(c)]. The MAE for mean and minimum NSATs

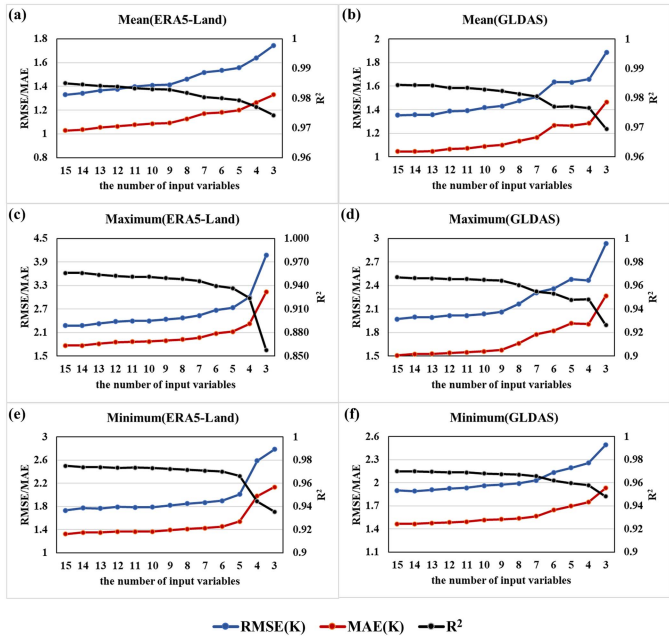

Fig. 6. Accuracy comparison of different input variables using models 1 and 2. (a), (c), and (e) Results for mean, maximum, and minimum NSAT estimation, respectively, during the period after 2000 using ERA5-Land related input (model 2). (b), (d), and (f) Corresponding results using GLDAS-related input (model 1).

was below 1.5 and 2 K, as represented by the green circles in Fig. 7(b) and (c). The RMSE in hotter months are smaller than those in cooler months (i.e., the RMSE for January and February are almost 2 K and 2.5 K for mean and minimum NSATs, respectively, while the RMSE is below 1.5 K for June and July for both mean and minimum NSATs). As shown in Fig. 7(e) and (f), differences between the extended and original product are small. Differences between RMSE lie within the range 0.10–0.7 K and 0.1–0.6 K for mean [see Fig. 7(e)] and minimum NSAT [see Fig. 7(f)], respectively. Differences lie within the range 0.10–0.50 K for MAE [see Fig. 7(e) and (f)]. Differences in the R^2 are very small. Although the accuracy of minimum and mean NSAT is higher in summer than in winter, this decreased accuracy is small compared with the original product.

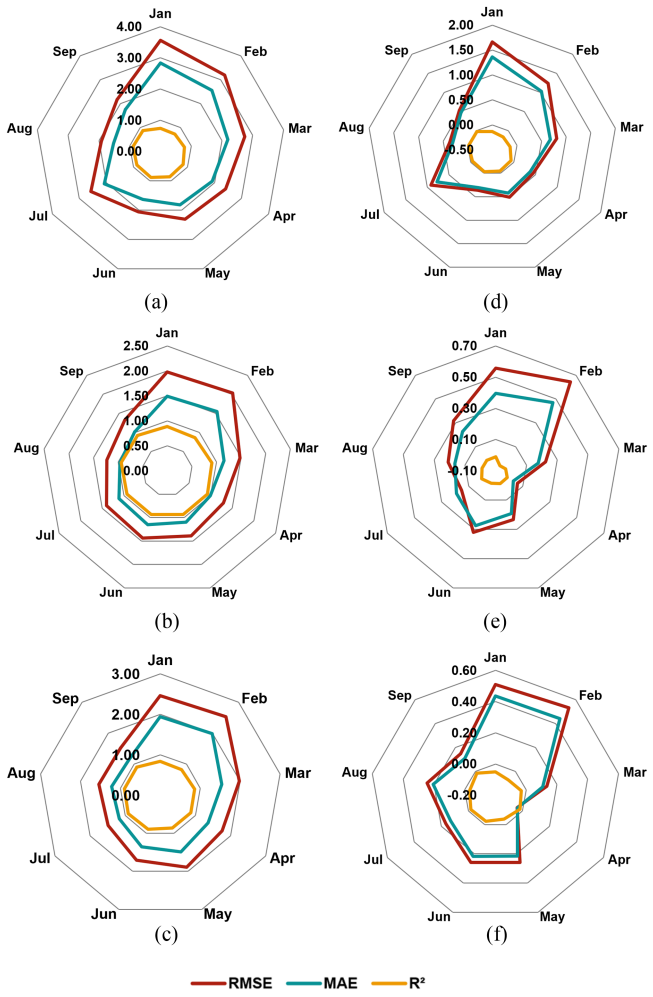

Fig. 7. Accuracy of NSAT estimation over different months of 2021. (a)–(c) Accuracy of maximum, mean, and minimum NSAT. (d)–(f) Differences in accuracy between the extended and original product for maximum, mean, and minimum NSAT. The unit for RMSE and MAE is K.

The RMSE vary from 1.5 to 3.5 K [red circle in Fig. 7(a)] for the extended maximum NSAT product, the MAE ranges from 1.5 to 3 K, and the R^2 is larger than 0.85 in most months [see Fig. 7(a)]. The R^2 decreases by less than 0.15 compared with that of the original product [see Fig. 7(d)]. Moreover, differences in MAE are in the range 0.3–1.35 K and RMSE differences lie within the range 0.4–1.6 K [see Fig. 7(d)]. The accuracy of maximum NSAT outside the original period lies below that of mean or minimum NSAT.

Overall, the accuracy of the temporally extended NSAT product remains satisfactory, especially for mean and minimum NSATs. In addition, the accuracy for different months of a year is different, with winter months showing lower accuracy compared with other seasons.

C. Evaluation of Spatial Extent Accuracy

To test the spatial migration ability of the NSAT estimation tool, the estimated NSAT over the Yangtze River Economic Belt as at September 1st, 2020 were estimated. The in situ observations over the Yangtze River Economic Belt were used to evaluate the estimated NSAT. Fig. 8(a) shows the spatial distribution of mean NSAT and Fig. 8(b) presents the quantitative evaluation results. The RMSE for maximum, mean, and minimum NSAT is 4.21 K, 2.72 K, and 3 K, respectively, and the MAE is 3.68 K, 2.3 K, and 2.6 K, respectively [see Fig. 8(b)]. The R^2 is larger than 0.8 for mean and minimum NSATs but is lower than 0.7 for maximum NSAT [see Fig. 8(b)]. The tool can be easily extended to estimate NSAT in any region, although spatial accuracy decreases compared with that of the estimated NSAT in the Yellow River Basin Region. The main reason for this is that the spatial heterogeneity of NSAT is nonnegligible [48], and the RF model for NSAT estimation strongly relies on the training data. Therefore, its spatial migration ability is limited.

D. Comparison With Other Products

From a spatial perspective, the three products generally exhibit consistency (a selected region is used to illustrate spatial details in Fig. 9). The seasonal variation trend is also consistent among the three products, albeit with some differences in detail. Notably, the NSAT product of Fang et al. [30] (first column of Fig. 9) has a coarser spatial resolution compared to the other two studies (last two columns of Fig. 9) due to its resolution of 0.1°. There is a noticeable mosaic effect in Fig. 9(a), (d), (g), and (j). When comparing the NSAT product of Chen et al. [27] with the NSAT product of this study, Fig. 9(b), (e), and (k) reveals more spatial details than Fig. 9(c), (f), and (l). This is primarily because Chen et al. [27] utilized MODIS LST in clear-sky conditions, which offer greater spatial detail compared to reanalysis or model simulation products. However, Fig. 9(h) also exhibits a mosaic effect similar to Fig. 9(g). In addition, Fig. 9(i) displays more spatial details than Fig. 9(g) and (h). Furthermore, the NSAT product of Fang et al. [30] and the NSAT product provided in this study exhibit seamless spatial details. In contrast, some missing pixels are evident in the NSAT product of Chen et al. [27], represented as blanks in Fig. 9(b) and (h).

Table IV compares the three NSAT products mentioned above. The products of Fang et al. [30] and Chen et al. [27] cover the whole region of China. They are spatially larger than this study and provide the opportunity for national scale investigation. NAST from Fang et al. [30] covers the period 1979–2018, while that from Chen et al. [27] covers 2003–2019. The study period of this article is from 1981 to 2020. This study provides a convenient NSAT estimation tool that can be used to easily predict NSAT at any time outside the time period stated. The spatial resolution of this study and that of Chen et al. [27] is 1 km, which is finer than the NSAT of Fang et al. [30]. The comparisons in Fig. 9 show that while our product may be less detailed than that of Chen et al. [27] in places, it is more stable on different days and is seamless in spatial. The three NSATs are all daily products. In addition, the study of Fang et al. [30] and this study provide the maximum, mean, and minimum NSAT, while only mean NSAT are generated by Chen et al. [27].

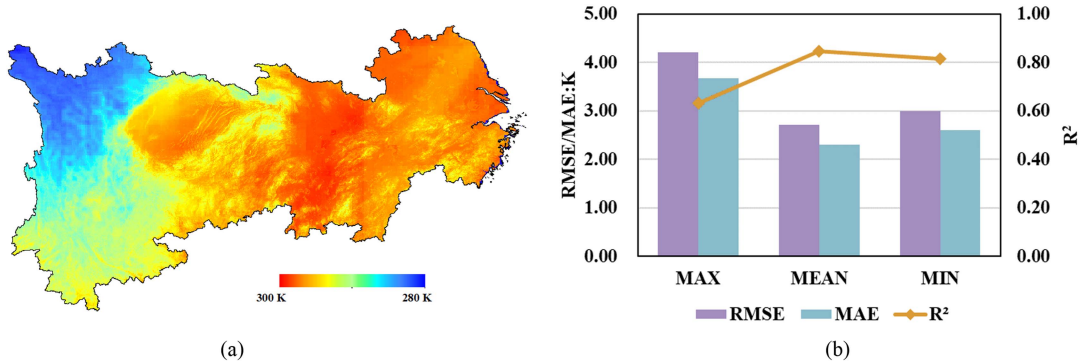

Fig. 8. Evaluation of spatially extended NSAT product over the Yangtze river economic belt on September 1st, 2020. (a) Spatial distribution of mean NSAT. (b) Quantitative evaluation results of each type of NSAT.

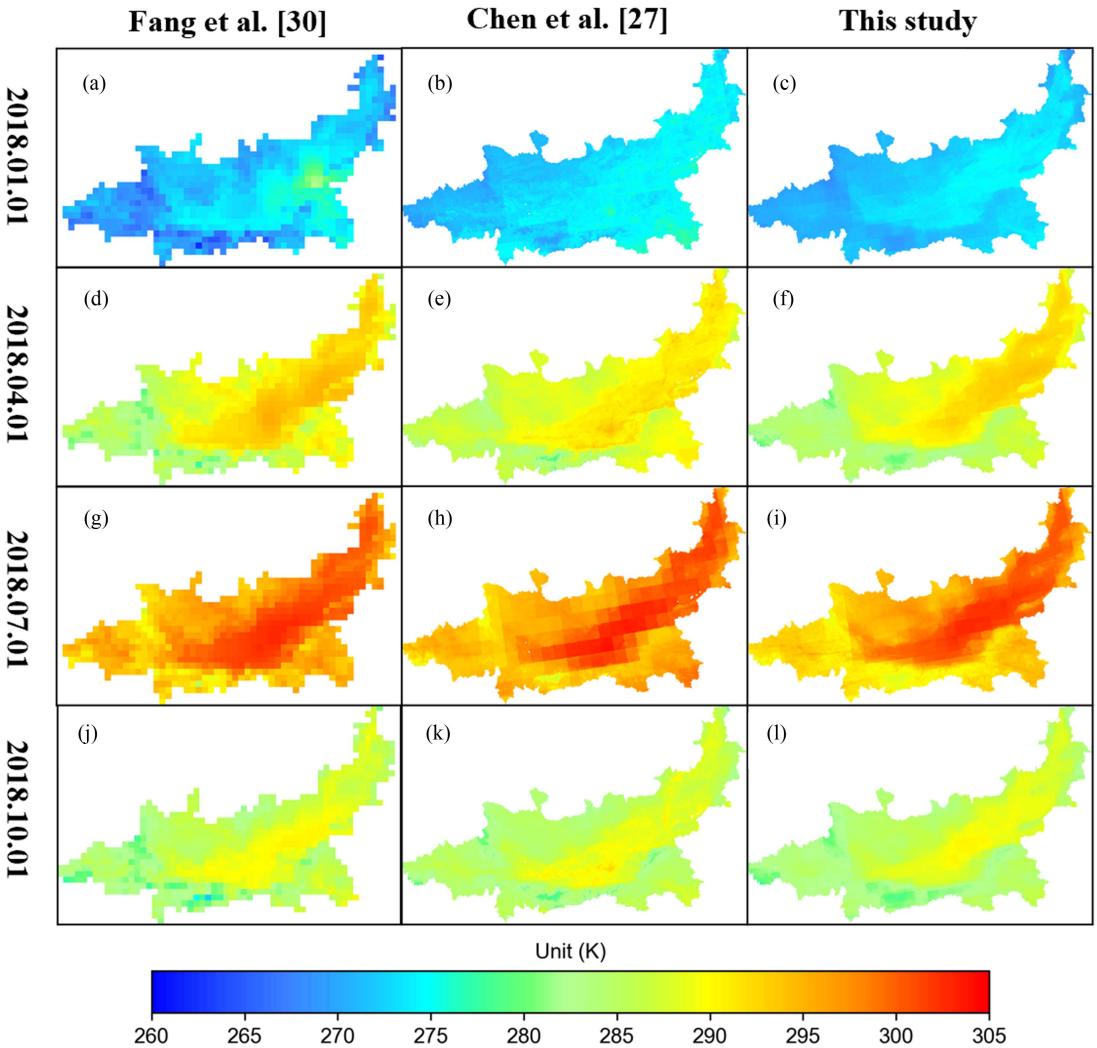

Fig. 9. Spatial distribution of the three NSAT products in different seasons. (a)–(c) January 1st, 2018. (d)–(f) April 1st, 2018. (g)–(i) July 1st, 2018. (j)–(l) October 1st, 2018.

TABLE IV
COMPARISONS AMONG THREE DAILY NSAT PRODUCTS

Product source	Fang et al. [30]	Chen et al. [27]	This study
Coverage	China	China	Yellow River Basin Region
Starting year	1979	2003	1981
Ending year	2018	2019	2020
Spatial resolution	0.1°	1 km	1 km
Temporal resolution	Daily	Daily	Daily
Maximum	Yes	/	Yes
Mean	Yes	Yes	Yes
Minimum	Yes	/	Yes
Extensibility	/	/	Yes

Compared with the NSAT product of Chen et al. [27], our product offers several advantages, including a longer temporal and seamless spatial coverage, greater stability across different seasons, and the availability of daily extreme temperature data. In comparison with the product of Fang et al. [30], which has a resolution of 0.1°, our study provides more detailed information at a resolution of 1 km. In addition, the inclusion of an NSAT extension tool in our study for public use enhances the flexibility and extendability of our product.

VI. CONCLUSION

In this article, a new technical framework is proposed to provide the ability to rapidly estimate long-term, 1-km daily seamless extreme and mean NSATs. The framework employs multiple sources of reanalysis and modeling products, remotely-sensed data, in situ observations, and other auxiliary data to establish NSAT estimated models. Three subsampling strategies were then designed to migrate the estimation model to the GEE platform to improve estimation efficiency. The most appropriate method was chosen for each period and type of NSAT to generate long-term fine-scale NSAT based on GEE. Subsequently, 40-year (from January 1st, 1981 to December 31st, 2020) 1-km daily seamless maximum, mean, and minimum NSAT products were developed using the framework. Tenfold cross validation shows that the RMSE, MAE, and R^2 for the maximum NSAT are less (larger for R^2) than 1.932 K, 1.486 K, and 0.968; less (larger for R^2) than 1.354 K, 1.035 K, and 0.984 for the mean NSAT; and less (larger for R^2) than 1.732 K, 1.322 K, and 0.975 for the minimum daily NSAT. The products can be used and downloaded from GEE (https://code.earthengine.google.com/c720b7c61c5da99ab5669b2ab70ca7df). To generate the NSAT product outside the time period or region covered by the products provided in this article, an easy-to-use tool entitled the NSAT estimation Tool (https://meilinggao888.users.earthengine.app/view/nsatestimation) was developed for users to customize their needs. The NSAT estimation tool demonstrates good migration performance temporally, although spatially extended accuracy decreases compared to that of the original products.

In summary, this study developed a high-quality NSAT product on the Yellow River Basin with seamless coverage, finer spatial and temporal resolution, and long-term continuity. Furthermore, an accompanying NSAT estimation tool was published for the first time to facilitate the extension of the product. Production of the NSAT product and the NSAT estimation tool relies on the GEE platform. All the data used in this study come from GEE except for the in situ data, making it straightforward to improve spatially extended accuracy once the in situ data in other regions are available in the future. This product and NSAT estimation tool are beneficial for environmental and climate research. Certain deficiencies will require addressing in the future, for example, the maximum NSAT is less accurate than mean and minimum NSAT in this study.

REFERENCES

[1] Q. Du, M. Zhang, S. Wang, C. Che, R. Ma, and Z. Ma, "Changes in air temperature over China in response to the recent global warming hiatus," *J. Geographical Sci.*, vol. 29, no. 4, pp. 496–516, 2019.
[2] X. Hu, M. Cai, S. Yang, and S. A. Sejas, "Air temperature feedback and its contribution to global warming," *Sci. China Earth Sci.*, vol. 61, no. 10, pp. 1491–1509, 2018.
[3] C. Huo-Po and S. Jian-Qi, "Drought response to air temperature change over China on the centennial scale," *Atmos. Ocean. Sci. Lett.*, vol. 8, no. 3, pp. 113–119, 2015.
[4] C. Lesk et al., "Stronger temperature–Moisture couplings exacerbate the impact of climate warming on global crop yields," *Nature Food*, vol. 2, no. 9, pp. 683–691, 2021.
[5] L. Li, Y. Zha, and R. Wang, "Relationship of surface urban heat island with air temperature and precipitation in global large cities," *Ecol. Indicators*, vol. 117, 2020, Art. no. 106683.
[6] B.-J. He, J. Wang, H. Liu, and G. Ulpiani, "Localized synergies between heat waves and urban heat islands: Implications on human thermal comfort and urban heat management," *Environ. Res.*, vol. 193, 2021, Art. no. 110584.
[7] Y. Huang, N. Jiang, M. Shen, and L. Guo, "Effect of preseason diurnal temperature range on the start of vegetation growing season in the Northern Hemisphere," *Ecol. Indicators*, vol. 112, 2020, Art. no. 106161.
[8] C. Bravo et al., "Air temperature characteristics, distribution, and impact on modeled ablation for the South Patagonia Icefield," *J. Geophysical Res., Atmos.*, vol. 124, no. 2, pp. 907–925, 2019, doi: 10.1029/2018jd028857.
[9] Z. Zhang and Q. Du, "Hourly mapping of surface air temperature by blending geostationary datasets from the two-satellite system of GOES-R series," *Int. Soc. Photogrammetry Remote Sens. J. Photogrammetry Remote Sens.*, vol. 183, pp. 111–128, 2022, doi: 10.1016/j.isprsjprs.2021.10.022.
[10] G. Zhang, S. Zhu, N. Zhang, G. Zhang, and Y. Xu, "Downscaling hourly air temperature of WRF simulations over complex topography: A case study of Chongli District in Hebei Province, China," *J. Geophysical Res., Atmos.*, vol. 127, no. 3, 2022, Art. no. e2021JD035542.
[11] J. Hrisko, P. Ramamurthy, Y. Yu, P. Yu, and D. Melecio-Vázquez, "Urban air temperature model using GOES-16 LST and a diurnal regressive neural network algorithm," *Remote Sens. Environ.*, vol. 237, 2020, Art. no. 111495, doi: 10.1016/j.rse.2019.111495.
[12] N. Nikolaou et al., "High-resolution spatiotemporal modeling of daily near-surface air temperature in Germany over the period 2000-2020," *Environ. Res.*, vol. 219, Feb. 2023, Art. no. 115062, doi: 10.1016/j.envres.2022.115062.
[13] D. Carrion et al., "A 1-km hourly air-temperature model for 13 northeastern U.S. states using remotely sensed and ground-based measurements," *Environ. Res.*, vol. 200, Sep. 2021, Art. no. 111477, doi: 10.1016/j.envres.2021.111477.

[14] Y. Yang, Q. You, Z. Jin, Z. Zuo, Y. Zhang, and S. Kang, "The reconstruction for the monthly surface air temperature over the Tibetan Plateau during 1901–2020 by deep learning," *Atmos. Res.*, vol. 285, Apr. 2023, Art. no. 106635, doi: 10.1016/j.atmosres.2023.106635.
[15] M. Gao, Z. Li, Z. Tan, H. Li, and J. Peng, "Use of Google Earth Engine to generate a 20-year 1 Km × 1 Km monthly air temperature product over yellow river basin," *IEEE J. Sel. Topics Appl. Earth Observ. Remote Sens.*, vol. 14, pp. 10079–10090, 2021, doi: 10.1109/jstars.2021.3116258.
[16] M. Zheng, J. Zhang, J. Wang, S. Yang, J. Han, and T. Hassan, "Reconstruction of 0.05° all-sky daily maximum air temperature across Eurasia for 2003–2018 with multi-source satellite data and machine learning models," *Atmos. Res.*, vol. 279, Dec. 2022, Art. no. 106398, doi: 10.1016/j.atmosres.2022.106398.
[17] R. S. dos Santos, "Estimating spatio-temporal air temperature in London (U.K.) using machine learning and earth observation satellite data," *Int. J. Appl. Earth Observ. Geoinf.*, vol. 88, 2020, Art. no. 102066, doi: 10.1016/j.jag.2020.102066.
[18] H. Shen, Y. Jiang, T. Li, Q. Cheng, C. Zeng, and L. Zhang, "Deep learning-based air temperature mapping by fusing remote sensing, station, simulation and socioeconomic data," *Remote Sens. Environ.*, vol. 240, 2020, Art. no. 111692, doi: 10.1016/j.rse.2020.111692.
[19] T. Zhang, Y. Zhou, L. Wang, K. Zhao, and Z. Zhu, "Estimating 1 km gridded daily air temperature using a spatially varying coefficient model with sign preservation," *Remote Sens. Environ.*, vol. 277, 2022, Art. no. 113072, doi: 10.1016/j.rse.2022.113072.
[20] L. Liu, H. Gu, J. Xie, and Y. P. Xu, "How well do the ERA-Interim, ERA-5, GLDAS-2.1 and NCEP-R2 reanalysis datasets represent daily air temperature over the Tibetan Plateau?," *Int. J. Climatol.*, vol. 41, no. 2, pp. 1484–1505, 2021.
[21] Y. Wang, G. Huang, and K. Hu, "Internal variability in multidecadal trends of surface air temperature over Antarctica in austral winter in model simulations," *Climate Dyn.*, vol. 55, no. 9, pp. 2835–2847, 2020.
[22] M. Rodell et al., "The global land data assimilation system," *Bull. Amer. Meteorological Soc.*, vol. 85, no. 3, pp. 381–394, 2004.
[23] J. Muñoz-Sabater et al., "ERA5-Land: A state-of-the-art global reanalysis dataset for land applications," *Earth Syst. Sci. Data*, vol. 13, no. 9, pp. 4349–4383, 2021.
[24] J. He et al., "The first high-resolution meteorological forcing dataset for land process studies over China," *Sci. Data*, vol. 7, no. 1, pp. 1–11, 2020.
[25] C. Shi, L. Jiang, T. Zhang, B. Xu, and S. Han, "Status and plans of CMA land data assimilation system (CLDAS) project," in *Proc. Eur. Geosci. Union Gen. Assem. Conf. Abstr.*, 2014, Paper 5671.
[26] R. Kistler et al., "The NCEP–NCAR 50-year reanalysis: Monthly means CD-ROM and documentation," *Bull. Amer. Meteorological Soc.*, vol. 82, no. 2, pp. 247–268, 2001.
[27] Y. Chen, S. Liang, H. Ma, B. Li, T. He, and Q. Wang, "An all-sky 1 km daily land surface air temperature product over mainland China for 2003–2019 from MODIS and ancillary data," *Earth Syst. Sci. Data*, vol. 13, no. 8, pp. 4241–4261, 2021.
[28] R. Li, T. Huang, Y. Song, S. Huang, and X. Zhang, "Generating 1 km spatially seamless and temporally continuous air temperature based on deep learning over Yangtze river basin, China," *Remote Sens.*, vol. 13, no. 19, 2021, Art. no. 3904, doi: 10.3390/rs13193904.
[29] H. Zhang, W. W. Immerzeel, F. Zhang, R. J. de Kok, S. J. Gorrie, and M. Ye, "Creating 1-km long-term (1980–2014) daily average air temperatures over the Tibetan Plateau by integrating eight types of reanalysis and land data assimilation products downscaled with MODIS-estimated temperature lapse rates based on machine learning," *Int. J. Appl. Earth Observ. Geoinf.*, vol. 97, 2021, Art. no. 102295, doi: 10.1016/j.jag.2021.102295.
[30] S. Fang et al., "Dataset of daily near-surface air temperature in China from 1979 to 2018," *Earth Syst. Sci. Data*, vol. 14, no. 3, pp. 1413–1432, 2022, doi: 10.5194/essd-14-1413-2022.
[31] J. Li, W. Sun, M. Li, and M. Linlin, "Coupling coordination degree of production, living and ecological spaces and its influencing factors in the Yellow River Basin," *J. Cleaner Prod.*, vol. 298, May 2021, Art. no. 126803, doi: 10.1016/j.jclepro.2021.126803.
[32] N. Gorelick, M. Hancher, M. Dixon, S. Ilyushchenko, D. Thau, and R. Moore, "Google Earth Engine: Planetary-scale geospatial analysis for everyone," *Remote Sens. Environ.*, vol. 202, pp. 18–27, 2017, doi: 10.1016/j.rse.2017.06.031.
[33] E. Vermote et al., "NOAA climate data record (CDR) of normalized difference vegetation index (NDVI), version 4," Nat. Ocean. Atmos. Admin. Nat. Clim. Data Cent, 2014.
[34] D. Yamazaki et al., "A high-accuracy map of global terrain elevations," *Geophysical Res. Lett.*, vol. 44, no. 11, pp. 5844–5853, 2017.
[35] T. G. Farr et al., "The shuttle radar topography mission," *Rev. Geophys.*, vol. 45, no. 2, pp. 1–33, 2007.
[36] M. Belgiu and L. Drăguţ, "Random forest in remote sensing: A review of applications and future directions," *Int. Soc. Photogrammetry Remote Sens. J. Photogrammetry Remote Sens.*, vol. 114, pp. 24–31, Apr. 2016.
[37] G. J. Mclachlan, K. A. Do, and C. Ambroise, *Analyzing Microarray Gene Expression Data*. Hoboken, NJ, USA: Wiley, 2004.
[38] D. S. Soper, "Greed is good: Rapid hyperparameter optimization and model selection using greedy k-fold cross validation," *Electronics*, vol. 10, 2021, Art. no. 1973.
[39] Y. Chen, R. Cao, J. Chen, L. Liu, and B. Matsushita, "A practical approach to reconstruct high-quality Landsat NDVI time-series data by gap filling and the Savitzky–Golay filter," *Int. Soc. Photogrammetry Remote Sens. J. Photogrammetry Remote Sens.*, vol. 180, pp. 174–190, Oct. 2021, doi: 10.1016/j.isprsjprs.2021.08.015.
[40] E. A. Njoku, P. E. Akpan, A. E. Effiong, and I. O. Babatunde, "The effect of station density in geostatistical prediction of air temperatures in Sweden: A comparison of two interpolation techniques," *Resour., Environ. Sustainability*, vol. 11, Sep. 2022, Art. no. 100092, doi: 10.1016/j.resenv.2022.100092.
[41] H. Theil, "A rank-invariant method of linear and polynomial regression analysis," *Indagationes Mathematicae*, vol. 12, pp. 85–91, 1950.
[42] P. K. Sen, "Estimates of the regression coefficient based on Kendall's tau," *J. Amer. Stat. Assoc.*, vol. 63, no. 324, pp. 1379–1389, 1968.
[43] A. Rosenfeld, M. Dorman, J. Schwartz, V. Novack, A. C. Just, and I. Kloog, "Estimating daily minimum, maximum, and mean near surface air temperature using hybrid satellite models across Israel," *Environ. Res.*, vol. 159, pp. 297–312, Nov. 2017, doi: https://doi.org/10.1016/j.envres.2017.08.017.
[44] Z. Zhang and Q. Du, "Merging framework for estimating daily surface air temperature by integrating observations from multiple polar-orbiting satellites," *Sci. Total Environ.*, vol. 812, Mar. 2022, Art. no. 152538, doi: 10.1016/j.scitotenv.2021.152538.
[45] F. Ji, Z. Wu, J. Huang, and E. P. Chassignet, "Evolution of land surface air temperature trend," *Nature Climate Change*, vol. 4, no. 6, pp. 462–466, Jun. 2014, doi: 10.1038/nclimate2223.
[46] D. B. Kattel, T. Yao, K. Ullah, and A. S. Rana, "Seasonal near-surface air temperature dependence on elevation and geographical coordinates for Pakistan," *Theor. Appl. Climatol.*, vol. 138, no. 3, pp. 1591–1613, Nov. 2019, doi: 10.1007/s00704-019-02899-5.
[47] S. L. Marcus, J. O. Dickey, and O. de Viron, "Air temperature and anthropogenic forcing: Insights from the solid earth," *J. Climate*, vol. 24, no. 2, pp. 569–574, 2011, doi: 10.1175/2010jcli3500.1.
[48] J. Cao, W. Zhou, Z. Zheng, T. Ren, and W. Wang, "Within-city spatial and temporal heterogeneity of air temperature and its relationship with land surface temperature," *Landscape Urban Plan.*, vol. 206, Feb. 2021, Art. no. 103979.

Meiling Gao received the B.Sc. degree in geographical information science from Chang'an University, Xi'an, China, in 2014 and the Ph.D. degree in cartography and geographic information system from Wuhan University, Wuhan, China, in 2019.

She is currently a Lecturer with the School of Geology Engineering and Geomatics, Chang'an University, Xi'an, China. Her main research interests include spatiotemporal data reconstruction and urban thermal environment.

Huihui Xu received the B.Sc. degree in geomatics engineering from the Shandong University of Technology, Zibo, China, in 2020 and the M.S. degree in geodesy and geoinformation science from Chang'an University, Xi'an, China, in 2023.

She specializes in research related to the heat environment.

Zhenyu Tan received the B.Sc. degree in geographical information science from Chang'an University, Xi'an, China, in 2013 and the Ph.D. degree in photogrammetry and remote sensing from Wuhan University, Wuhan, China, in 2019.

He is a Lecturer with the College of Urban and Environmental Sciences, Northwest University, Xi'an, China. His main research interests include remote sensing environment monitoring, data fusion, and deep learning in geosciences.

Zhenhong Li (Senior Member, IEEE) received the B.Eng. degree in geodesy from the Wuhan Technical University of Surveying and Mapping (now Wuhan University), Wuhan, China, in 1997 and the Ph.D. degree in GPS, geodesy, and navigation from University College London, London, U.K., in 2005.

He is currently a Professor of imaging geodesy with the College of Geological Engineering and Geomatics, Chang'an University, Xi'an, China, Vice Director of the Key Laboratory of Loess, Xi'an, and the Director of the Key Laboratory of Western China's Mineral Resource and Geological Engineering, Ministry of Education, Xi'an. He is also the Principal Investigator of the Generic Atmospheric Correction Online Service for interferometric synthetic aperture radar. His research interests include imaging geodesy and its applications to geohazards (e.g., earthquakes, landslides, and land subsidence) and ecoenvironment.

Dr. Li is a Fellow of the International Association of Geodesy and an Associate Editor for Advances in Space Research and Remote Sensing.

Guijun Yang received the Ph.D. degree in cartography and geography information system from the Institute of Remote Sensing Applications, Chinese Academy of Sciences, Beijing, China, in 2008.

He is currently a Professor with the College of Geological Engineering and Geomatics, Chang'an University, Xi'an, China. His research interests include radiative transfer modeling and quantitative remote sensing in agriculture and forestry.